Supporting Information

Yanshen Li[a,b], David Quéré[c], Cunjing Lv[a,d], Quanshui Zheng[a,b,e,1]

[a]Department of Engineering Mechanics, Tsinghua University, Beijing 100084, China.
[b]Center for Nano and Micro Mechanics, Tsinghua University, Beijing 100084, China.
[c]Physique et Mécanique des Milieux Hétérogènes, UMR 7636 du CNRS, ESPCI, 75005 Paris, France.
[d]Institute for Nano- and Microfluidics, Center of Smart Interfaces, Technische Universität Darmstadt, Alarich-Weiss-Straße 10, 64287 Darmstadt, Germany.
[e]Applied Mechanics Lab, and State Key Laboratory of Tribology, Tsinghua University, Beijing100084, China.

Contents

1. Sample preparation

a) OTS coating and Glaco coating

The samples, silicon substrates and glass slides (7101, Sailer, China), are first washed in acetone, ethanol, isopropanol and deionized (DI) water, successively. After being dried with clean nitrogen gas, they are treated by oxygen plasma (Femto SLCE, Diener Electronic, Germany) at 30 watts for 2 hours, and immediately placed for 20 min in a 0.4% v/v solution of octadecyltrichlorosilane (OTS) in hexadecane. The samples are then dipped in chloroform for 15 min to remove any residual organics or liquids, and in ethanol for 15 min. They are finally dried with clean nitrogen gas, which completes the OTS coating procedure.

Silicon substrates can also be treated with a commercial superhydrophobic coating (Glaco Mirror Coat "Zero", Soft 99, Japan) consisting of hydrophobic nanoparticles dispersed in isopropanol. Substrates are drawn out of the dispersion, dried in air and consolidated at 150°C for 15 min. Dip-coating and heating steps are repeated three times (1). Glass slides (7101, Sailer, China) used as pressing plates are treated the same way.

b) Contact angle measurements

Advancing/receding contact angles of water/mercury on flat substrates are measured by displacing a drop with diameter smaller than its capillary length. The drop is pushed horizontally by a Glaco-coated glass plate and motion is slow (50 μm/s), which provides quasi-static angles. Advancing and receding contact angles are measured simultaneously from side views such as displayed in Figure S1.

Contact angles measured for the different samples used in this study are reported in Table S1. We denote them as "intrinsic" contact angles, since they characterize the flat materials, without micropillars.

In the accompanying paper we also report contact angles on surfaces with hydrophobic pillars, which are measured from side views of backlighted drops. As drops are squeezed, water (or mercury) adopts an advancing angle independent of the confinement as long as the drop remains in the Cassie state. This is shown in Figure S2, where a millimeter-size water drop is pressed against a substrate with hydrophobic pillars. Both the high value of the angle (162° ± 1° in both cases) and the light passing below the drop are signatures of the Cassie state.

c) Morphologies of the microposts

Silicon substrates with square arrays of microposts are fabricated by photolithography. For each morphology, two identical copies are made, and coated respectively with OTS and Glaco, using the above-described procedures. Morphologies of the corresponding substrates

[1]To whom correspondence should be addressed.
Email: zhengqs@tsinghua.edu.cn.

used in Fig. 2 are characterized by Scanning Electronic Microscopy (SEM) (JSM-IT300, JEOL Japan) and Atomic Force Microscopy (AFM) (NTEGRA Aura, NT-MDT, Russia). We can see in Figure S3 that the Glaco-coated posts have slightly enlarged tops and larger surface roughness (the root mean square roughness at the bottom of the Glaco and OTS coated substrates is 85 nm and 7.9 nm, respectively).

d) Geometries of the silicon substrates

The characteristics of the silicon substrates used in the paper are listed in Table S2, which gives the side length/diameter a of pillars with a square/circular section, the post spacing b, the post height h, the surface fraction $f = a^2/(a + b)^2$, and the roughness factor $r = 1 + 4hf/a$. The two latter quantities are given for square pillars and they become $f = \pi a^2/4(a + b)^2$ and $r = 1 + 4hf/a$ for circular pillars.

e) Treatments of the silicon substrates for tuning their contact angles with mercury

The variability of the contact angle of mercury was obtained from five surface treatments. We list these treatments in Table S3 and indicate the corresponding contact angles ranked following decreasing values. (1) OTS treatment is the same as described above. (2) We use directly silicon substrate without any treatment. (3) For "aged air plasma", the sample is stored in clean air at room temperature for one week after treatment by air plasma. (4) For "air plasma": after cleaning, the substrate is plasma-exposed at 30 watts for 30 min using air. (5) O_2 plasma: after cleaning, the substrate is oxygen-plasma treated at 30 watts for 30 min using pure oxygen.

f) Nanostructured CuO surface

Superhydrophobic CuO nanostructures on copper were made in two steps (2): (i) Cleaning: a copper brick is first ultrasonically cleaned in acetone for 10 min, and secondly in ethanol, isopropanol and DI water, successively. Then the brick is dipped into a 2M solution of hydrochloric acid for 10 min to remove the native oxide film at the surface, and then triple-rinsed with DI water and dried with clean nitrogen gas. (ii) Oxidation: nanostructured CuO films are formed by immersing the cleaned bricks into a hot (96 ± 3°C) alkaline solution composed of $NaClO_2$, NaOH, $Na_3PO_4{\bullet}12H_2O$, and DI water (3.75:5:10:100 wt%) for 20 min. During the oxidation process, a thin (≈ 300 nm) Cu_2O layer forms and gets reoxidized into sharp, knife-like CuO structures, as shown in Figure S4. Bricks are finally rinsed with DI water three times, and dried with nitrogen. The copper plate coated with CuO nanostructures has contact angles $\theta_a = 163° \pm 3°$ and $\theta_r = 161° \pm 2°$ for mercury, with a contact angle hysteresis less than 2°.

2. Calculation of the interfacial energy of compressed drops

There have been a number of researches on the shape of the advancing meniscus when a liquid is spreading through pillar arrays. For example, Rong Xiao and co-workers found that the meniscus shape between pillars should be concave by employing Surface Evolver simulations and interference microscopy (3), and Pirat carried out simulations to investigate the shape of the advancing meniscus (4). Besides, Courbin (5) and Peter (6, 7) analyzed the macroscopic wetted area, which could adopt circular, square, or polygonal depending on the structures on the substrate.
In our case, menisci are rather receding, and we calculate the interfacial energy of a drop as the product of surface energies by corresponding surface areas measured for each interface. Since experiments are carried out at room temperature, we adopt the values of the water-air and mercury-air surface tension as 72.8 mN/m and 425.4 mN/m, respectively. The solid-liquid interfacial energies are calculated from Young's formula $\gamma_{SL} - \gamma_{SV} = -\gamma\cos\theta_E$, where we take $\theta_E = (\theta_a + \theta_r)/2$ for the equilibrium contact angle of the liquid on the different materials. The distances R_t, R_S, R_W and R are defined in Figure S5 and can all be extracted from side views. They respectively correspond to the liquid/plate contact radius, apparent liquid substrate contact radius, Wenzel contact radius and the cross-sectional radius at arbitrary height.

The drop-plate interfacial energy is $U_{top} = \pi R_t^2\gamma\cos\theta_{E,top}$, the liquid-air interfacial energy between the plate and the substrate (yellow curves in Fig. S5) can be calculated as $U_{side} = \gamma\int_0^{s(z)} 2\pi R\mathrm{d}s$, a quantity integrated over the curvilinear coordinate s. In practice, the resolution ds is given by the pixel size, that is, 8.5 μm. The interfacial energy of the drop-substrate area is calculated as below:

(i) If the drop is in a mixed Cassie-Wenzel state or in a Wenzel state:

$$U_{bottom} = \pi(R_S^2 - R_W^2)(1-f)\gamma - \pi(R_S^2 - R_W^2)f\gamma\cos\theta_{E,bottom} - \pi R_W^2\gamma r\cos\theta_{E,bottom}$$

(ii) If the drop is in Cassie state:

$$U_{bottom} = \pi R_S^2\gamma(-f\cos\theta_{E,bottom} + 1 - f)$$

The total interfacial energy is finally:

$$U = U_{top} + U_{side} + U_{bottom} \qquad \textbf{[S1]}$$

As an example, we show in Figure S6*A* the interface profiles extracted from the 6th frame in Fig. S8*C* after using image processing toolbox by Matlab. The liquid-air interface between the plate and the substrate is shown in Figure. S6*B* with more detail. The position of the liquid-plate interface is taken at the place where the drop

and its mirror image intersect, and it can be determined by the local minimum of the radius R_v. The position of the pillar tops is read manually.

Parameters such as R_t, R_v, and R_S are finally extracted, while R_W and R are measured manually. The total interfacial energy of the drop is calculated by **Eq. S1.**

3. Pause in the lifting phase

During the lifting process shown in Fig. 2, it is worth noting that if we stop the plate when the drop is in the mixed Cassie-Wenzel state, the dewetting process stops as well. Dewetting only restarts if we lift the plate further. Figure S7 shows five successive snapshots for water on a Glaco-coated substrate (a = 19 μm, b = 101 μm, h = 100 μm) where time indicates the duration of the pause. It is observed that the mixed Cassie-Wenzel state indeed remains frozen as long as the squeezing distance remains constant. We just notice a slight reduction in drop volume after 35 s due to evaporation.

4. Additional experiments

a) Two sets of additional experiments with different parameters

Experiment Set 1. Figure S8 shows an experiment similar to those in Fig. 2, where pillars are spaced by b = 101 μm instead of 80 μm (width a and height h are the same as in Fig. 2). The corresponding force and energy curves are shown in Fig. S9. The essential features are the same as those shown in Fig. 2.

Experiment Set 2. Figure S10 shows the results of an experiment similar to that in Fig. S8, except that the upper plate is OTS-treated, which yields water contact angles θ_a = 114° ± 2° and θ_r = 80° ± 2°. The higher adhesion to the upper plate generates a force that tends to detach the drop from the Wenzel state in the lifting stage. Despite this contrast with the experiments reported in the accompanying paper, we see no qualitative difference in the various phenomena, and our conclusions remain unchanged.

b) Experiments with glycerol

Figure S11 shows that glycerol dewets in the releasing state in the same manner as water, despite a much higher viscosity. The pillars have a width a = 19 μm and a spacing b = 80 μm. Glycerol has a lower surface tension than water, and thus a smaller receding angle on Glaco-coated silicon, namely θ_r = 122° ± 2°. This receding angle on this substrate does not satisfy **Eq. 1**, so that we have to make the surface energy of Glaco coating even smaller to observe the W2C transition. We first treat the Glaco-coated silicon substrate with oxygen plasma for 30 min (which makes the surface superhydrophilic) and then place the sample in a 0.5 mM solution of FOTS (1H,1H,2H,2H-perfluorooctyltrichlorosilane) in a mixture of hexadecane and chloroform (4:1) for 15 min (8). After cleaning the substrate with isooctane, isopropanol and DI water, we measure the receding contact angle for glycerol of θ_r = 139° ± 3°, higher than without FOTS-coating. The advancing angle on this surface is θ_a = 163° ± 1°, and thus we have θ_E = 151° ± 2°.

5. Local energy barrier in the W2C transition

As evidenced in Fig. 2, water and mercury in a monostable Cassie state dewet pillars from the side, in a fashion similar to that of a liquid progressing within textured surfaces (4, 5). As sketched in Figure S12*A*, the progression of the Cassie state (seen from the top) implies that new liquid-air interfaces advance and meet at the corner between pillars. Liquid within pillars is swept away as interfaces later move to positions 3 and 4. Position 3 progresses further to 5, where it can merge with interface 6, and so on.

During this process, one key step is how the two interfaces dewet the vertical sharp edge S (Fig. S12). As shown by Gibbs, a sharp edge can pin the contact line (9). In the case of a square pillar, this pinning induces variability of the contact angle by 90°. Therefore, interface F' at the corner needs to be parallel to interface F'' to move further. In Fig. S12, we have θ < 135°, and the two interfaces 1 and 2 will merge and dewet the pillar as soon as interfaces meet the symmetry plane O.

In order to look more carefully at the condition for menisci to merge, we use Surface Evolver. This software, developed by Brakke (10), is especially designed to find the minimum energy and shape of a surface subjected to a given set of constraints, and it has been classically employed to determine the shape of droplets on various kinds of substrate (11-19). A typical starting point of the simulation is shown in Figure S13, where red squares represent pillars, and blue stripes show the liquid-air interfaces in the Cassie state. For the sake of clarity, pillar walls and liquid-solid interfaces are not shown. Only menisci within the pillars are considered, and the Wenzel region covers 4 × 4 pillars at the center of the domain. The drop is ignored so the pressure difference through the interface is zero. Contact angles on all walls are set to θ. Pillar side length a, spacing b, height h and contact angle θ are varied. This design has 4 symmetry planes so that we restrict the simulation to 1/8 of the domain.

Mimicking the experiments in Fig. 4 for f = 0.44, we choose a = 2b and h = a. Figure S14 shows the equilibrium shape of the menisci for different contact angles. At low θ, the menisci do not reach the sharp edge

of the pillar (Fig. S14*A*-*B*). As θ increases, the menisci can reach these edges on which they pin, which makes vertical the bottom of each meniscus. Owning to the matching condition of an obtuse angle with the bottom, the menisci protrude outwards and become convex so that interfaces will eventually merge (Fig. S14*C*-*D*). For larger angles, menisci are more convex and they easily merge (Fig. S14*E*-*F*). We define α as the angle between the bottom contact line and the wall (Fig. S14*B*), which allows us to propose as a criterion for menisci to merge: $\alpha < 45°$ (Fig. S14*E*), if we have $\theta < 135°$. When $\theta > 135°$ (which can be the case for mercury), the criterion becomes $\alpha < \theta - 90°$.

We conducted a series of simulations to see how α varies as a function of θ, the result of which is plotted in Figure S15. In each case, α is obtained from the analysis of the bottom contact line as can be seen for example in Fig. S14*B*. The mesh in the simulation is chosen so to have between 150 and 250 data points along the contact line between pillars, which yields a precision of about 3° for α. It is found that α monotonously decreases with θ: as mentioned earlier, as contact angles get larger, interfaces become more and more convex. In a first case (Fig. S15*A*), we consider $a = 2b$ and $h = a$; in a second case (Fig. S15*B*), we consider $a = 4b$ and $h = a$. In both cases, the critical value $\alpha = 45°$ is reached for comparable contact angles of around 104°, as indicated by a green solid line. If the contact angle if larger than this value (most cases in Fig. 4), the Cassie state can propagate without being pinned at the edges. For water and simple pillars (no sub-texture), contact angle can be smaller than this value, and pinning on the pillar edges can impede the W2C transition. This is made visible in Fig. S15 where we show with a dashed line the value of the critical angle for W2C transition calculated for **Eq. 1**. In case *A*, this angle coincides with $\theta(45°)$, which implies that local pinning does not affect the transition; in case *B*, it is much smaller than $\theta(45°)$, which means that the transition will be dictated by the depinning from the pillar edges.

These findings support the phase diagram reported in Fig. 4. We understood that pinning does not impede W2C transition at $f = 0.44$. In particular, further simulations confirm that at larger pillar spacing ($b > a/2$, $f < 0.44$), α remains smaller than 45° as long as **Eq. 1** is satisfied, as reported in Figure S16.

We finally investigated the influence of the pressure on this local energy barrier. Drops with different radii are considered, and it is found in Figure S17 that the critical angle of depinning (that is, $\theta(45°)$) slightly increases as the drop radius decreases. For instance, this angle passes from ~104° to ~106° when the drop radius changes from infinite to 1 mm (where the latter value corresponds to our experiment).

1. Vakarelski IU, Patankar NA, Marston JO, Chan DYC, Thoroddsen ST (2012) Stabilization of Leidenfrost vapour layer by textured superhydrophobic surfaces. *Nature* 489(7415):274-277.
2. Miljkovic N, et al. (2012) Jumping-droplet-enhanced condensation on scalable superhydrophobic nanostructured surfaces. *Nano Lett* 13(1):179-187.
3. Xiao R, Enright R, Wang EN (2010) Prediction and optimization of liquid propagation in micropillar arrays. *Langmuir* 26(19):15070-15075.
4. Pirat C, et al. (2008) Multiple time scale dynamics in the breakdown of superhydrophobicity. *Europhys Lett* 81(6):66002.
5. Courbin L, et al. (2007) Imbibition by polygonal spreading on microdecorated surfaces. *Nat Mater* 6(9):661-664.
6. Peters AM, et al. (2007) Spontaneous breakdown of superhydrophobicity. *Phys Rev Lett* 99(15):156001.
7. Peters AM, et al. (2009) Cassie-Baxter to Wenzel state wetting transition: Scaling of the front velocity. *Eur Phys J E Soft Matter* 29(4):391-397.
8. Cao L, Price TP, Weiss M, Gao D (2008) Super Water- and Oil-Repellent Surfaces on Intrinsically Hydrophilic and Oleophilic Porous Silicon Films. *Langmuir* 24(5):1640-1643.
9. Quéré D (2008) Wetting and roughness. *Annu Rev Mater Res* 38:71-99.
10. Brakke KA (1992) The Surface Evolver. *Exp Math* 1(2):141-165.
11. Brandon S, Wachs A, Marmur A (1997) Simulated Contact Angle Hysteresis of a Three-Dimensional Drop on a Chemically Heterogeneous Surface: A Numerical Example. *J Colloid Interface Sci* 191(1):110-116.
12. Brandon S, Haimovich N, Yeger E, Marmur A (2003) Partial wetting of chemically patterned surfaces: The effect of drop size. *J Colloid Interface Sci* 263(1):237-243.
13. Chatain D, Lewis D, Baland J, Carter WC (2006) Numerical Analysis of the Shapes and Energies of Droplets on Micropatterned Substrates. *Langmuir* 22(9):4237-4243.
14. Dorrer C, Rühe J (2007) Contact Line Shape on Ultrahydrophobic Post Surfaces. *Langmuir* 23(6):3179-3183.
15. Kusumaatmaja H, Yeomans JM (2007) Modeling contact angle hysteresis on chemically patterned and superhydrophobic surfaces. *Langmuir* 23(11):6019-6032.
16. Santos MJ, White JA (2011) Theory and Simulation of Angular Hysteresis on Planar Surfaces. *Langmuir* 27(24):14868-14875.
17. Matsui H, Noda Y, Hasegawa T (2012) Hybrid Energy-Minimization Simulation of Equilibrium Droplet Shapes on Hydrophilic/Hydrophobic Patterned Surfaces. *Langmuir* 28(44):15450-15453.
18. Promraksa A, Chen L (2012) Modeling contact angle hysteresis of a liquid droplet sitting on a cosine wave-like pattern surface. *J Colloid Interface Sci* 384(1):172-181.
19. Zhong Y, Jacobi AM, Georgiadis JG (2013) Effects of surface chemistry and groove geometry on wetting characteristics and droplet motion of water condensate on surfaces with rectangular microgrooves. *Int J Heat Mass Transf* 57(2):629-641.

Table S1. Intrinsic contact angles for the different liquids and samples used in our study.

Liquid	Material	Coating	θ_a (deg)	θ_r (deg)
Water	Glass	OTS	114° ± 2°	80° ± 2°
Water	Silicon	OTS	113° ± 3°	91° ± 2°
Water	Glass	Glaco	167° ± 2°	159° ± 2°
Water	Silicon	Glaco	164° ± 2°	150° ± 3°
Mercury	Glass	Glaco	167° ± 2°	162° ± 2°
Mercury	Silicon	OTS	165° ± 2°	137° ± 4°

Table S2. Characteristics of the silicon substrates.

No.	Shape	a (μm)	b (μm)	h (μm)	f	r
1	Square	100	50	100	0.44	2.8
2	Circular	100	33	100	0.44	2.8
3	Square	100	75	100	0.33	2.3
4	Circular	100	55	100	0.33	2.3
5	Square	100	100	100	0.25	2.0
6	Circular	100	77	100	0.25	2.0
7	Square	100	120	100	0.21	1.8
8	Circular	100	95	100	0.21	1.8
9	Square	100	150	100	0.16	1.6
10	Circular	100	122	100	0.16	1.6
11	Square	100	200	100	0.11	1.4
12	Circular	100	166	100	0.11	1.9
13	Square	19	80	100	0.04	1.8
14	Square	19	101	100	0.03	1.5

Table S3. Treatments and corresponding contact angles of mercury on flat substrates.

No.	Method	θ_a	θ_r
1	OTS	165° ± 2°	137° ± 4°
2	None	144° ± 4°	123° ± 3°
3	Aged air Plasma	144° ± 1°	116° ± 3°
4	Air plasma	137° ±2°	107° ± 3°
5	O_2 plasma	132° ± 1°	97° ± 3°

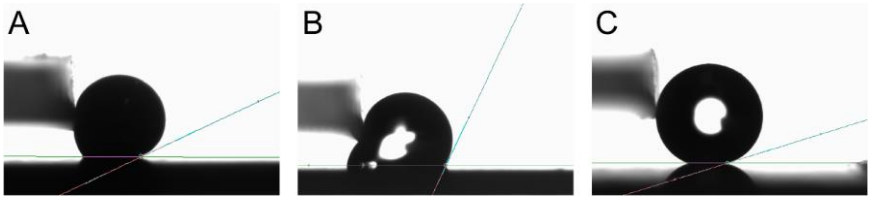

Fig. S1. Measurement of advancing/receding contact angles on flat surfaces by moving the droplet horizontally with a non-wetting plate coated by Glaco. (*A*) Mercury on OTS-coated silicon. (*B*) Water on OTS-coated silicon. (*C*) Water on Glaco-coated silicon.

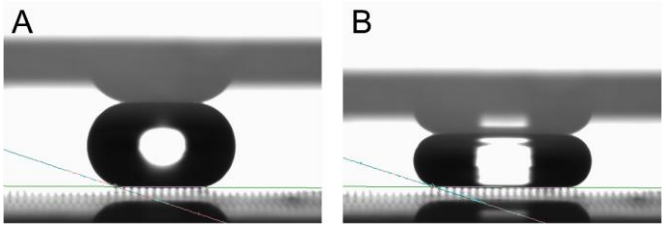

Fig. S2. Measurement of advancing contact angle on surface with pillars, by pressing the drop with an upper plate with a Glaco-coating. The photos show two degrees of confinement, in the Cassie state.

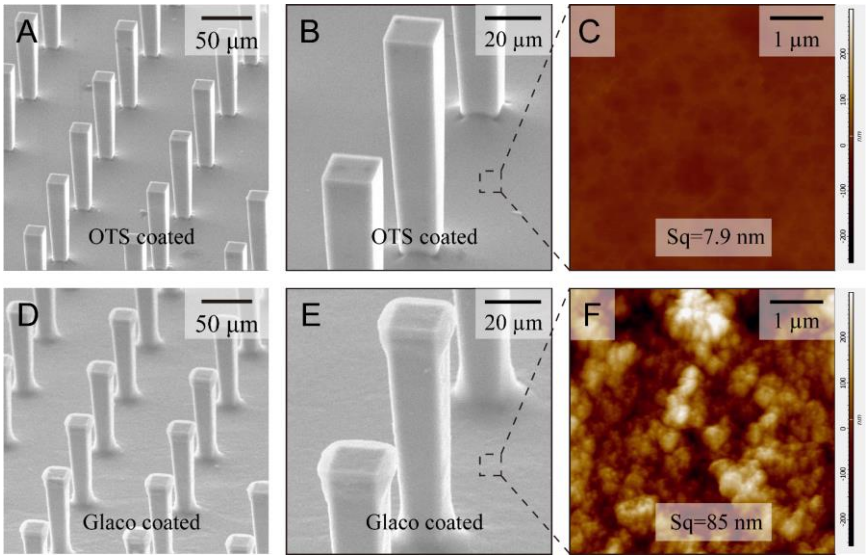

Fig. S3. OTS and Glaco-coated textured silicon substrates. (*A-B*) SEM images; (*C*) AFM image of the OTS-coated substrate textured by pillars with side length a = 19 µm, spacing b = 80 µm and height h = 100 µm. The root mean square roughness at the bottom of the substrate is 7.9 nm. (*D-F*) Similar images of this substrate coated with Glaco. The root mean square roughness at the bottom of the substrate is 85 nm.

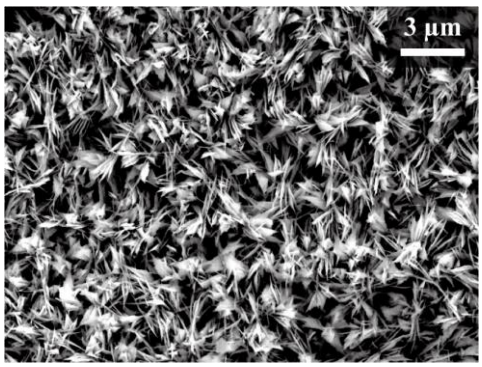

Fig. S4. SEM image of the CuO nanostructure.

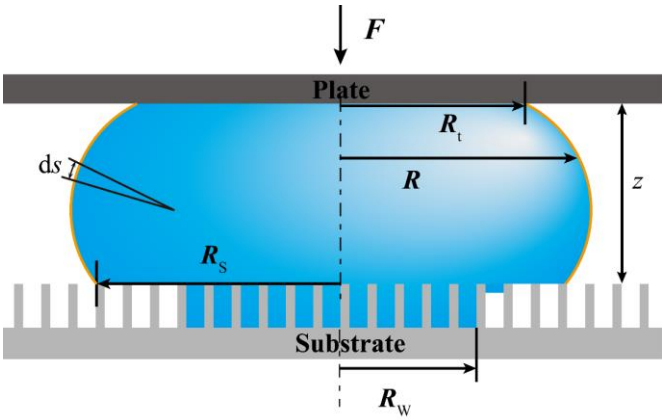

Fig. S5. Geometrical parameters extracted from experiments and defined in this sketch.

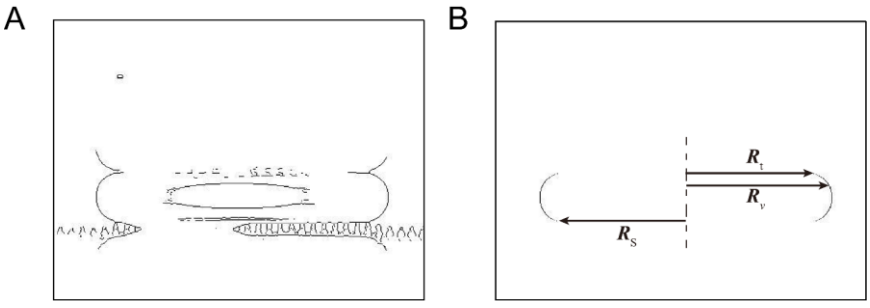

Fig. S6. Drop outline and extraction of geometrical parameters. (*A*) Outline extracted from the 6th frame of Fig. S8*C*. (*B*) Outline of the liquid-air interface between the plate and the substrate extracted from Fig. S6*A*.

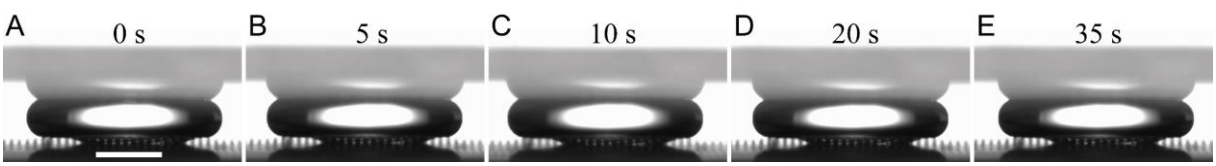

Fig. S7. Pause during the lifting process, in the mixed Cassie-Wenzel state. Time in each figure indicates the duration of the pause and the drop is observed to remain the same. The scale bar shows 1 mm.

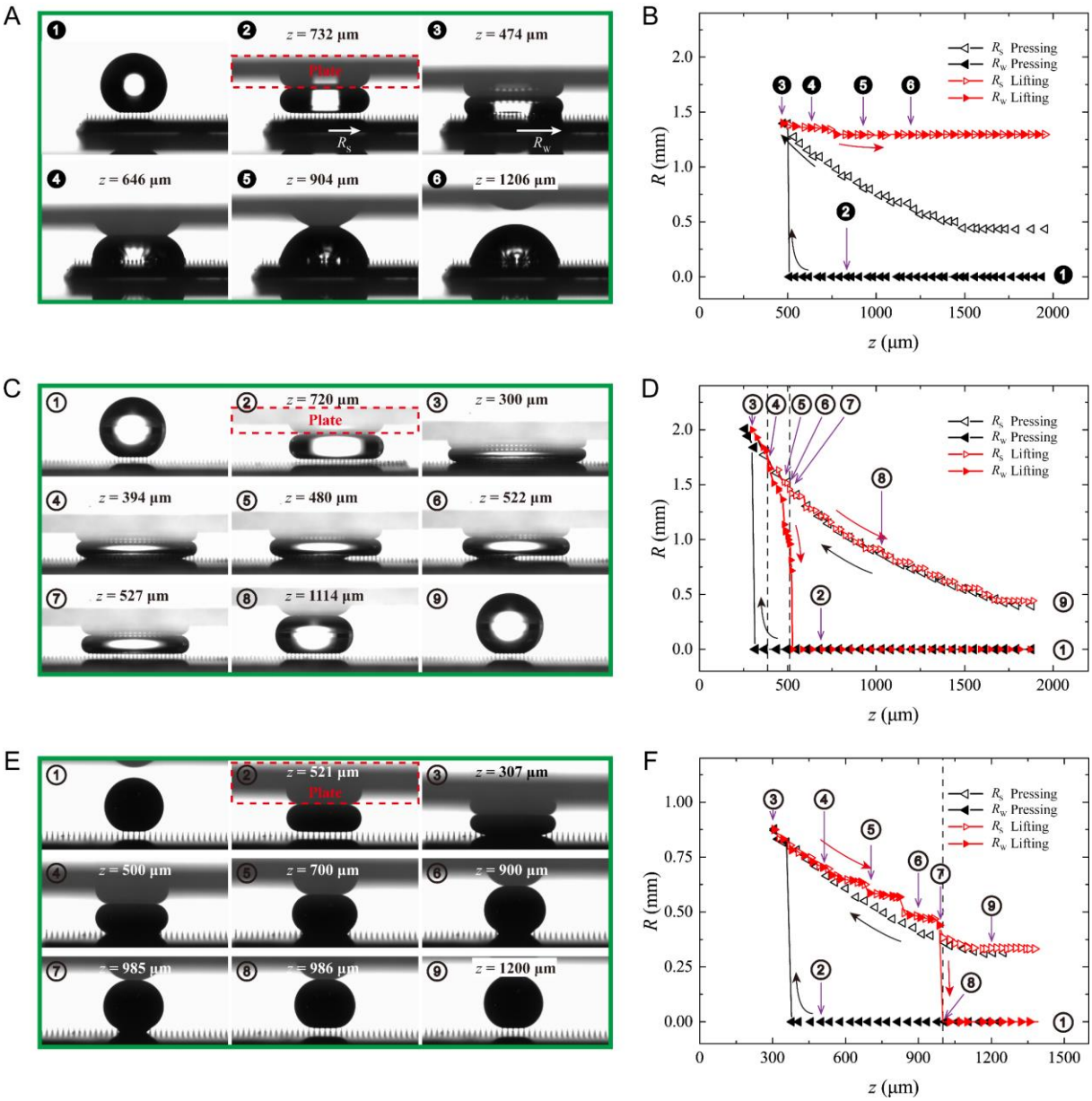

Fig. S8. States and contact radii of a drop squeezed against a textured surface. (*A*) Snapshots for water (R = 1 mm) on silicon pillars (h = 100 µm and b = 101 µm) treated with OTS. OTS-treated silicon yields water contact angles $\theta_a = 113° \pm 3°$ and $\theta_r = 91° \pm 2°$. Corresponding movie is Movie S4. The drop in the Cassie state (❶) is pressed (❷) until reaching the Wenzel state (❸). Upon lifting, it gets stretched (❹,❺) but remains pinned (❻). (*B*) Drop radius as a function of the distance z between the plate and substrate. R_s (with empty triangles) denotes the radius of contact between the drop and the top of the substrate, and R_w (with full triangles) denotes the radius of the Wenzel contact. Symbols are black and left-pointed in the pressing stage, and they are red and right-pointed in the lifting stage. The states corresponding to Fig. S8*A* are marked with numbers. (*C*) Same experiment after treating the same substrate with Glaco ($\theta_a = 164° \pm 2°$ and $\theta_r = 150° \pm 3°$). Corresponding movie is Movie S5. The initial Cassie drop (①) is pressed (②) so to reach the Wenzel state (③). Upon lifting, the drop first shrinks (④) before water dewets the pillars from the edge (⑤⑥); this mixed state eventually leads to a compressed Cassie state (⑦) conserved over further lifting (⑧⑨). (*D*) Drop radii R_W and R_S as functions of z. The two vertical dashed lines indicate the boundaries of the mixed state and numbers refer to Fig. S8*C*. (*E*) Same experiment as Fig. S8*A* with mercury (R = 0.66 mm, $\theta_a = 165 \pm 2°$, $\theta_r = 137 \pm 4°$). Corresponding movie is Movie S6. The sequence is comparable to that in *C*. (*F*) R_W and R_S as functions of z. The drop being small and only wets a few pillars at the start of the mixed stage, it undergoes a sudden change from Wenzel to Cassie state, and R_W drops suddenly at z = 986 µm. The vertical dashed line indicate the position where the transition happens. Numbers refer to Fig. S8*E*.

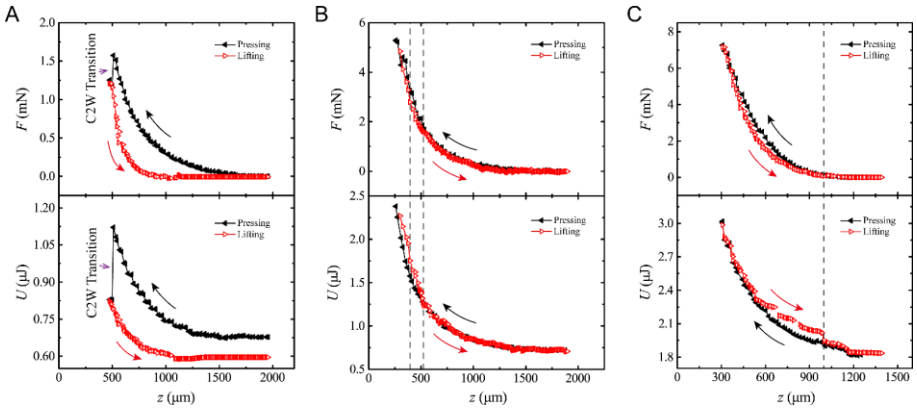

Fig. S9. Force and total energy curves of the drop. (*A*), (*B*) & (*C*) corresponds to Fig.S8*A*, *C*, *E*, respectively. Dashed lines mark the bounds of the W2C transition.

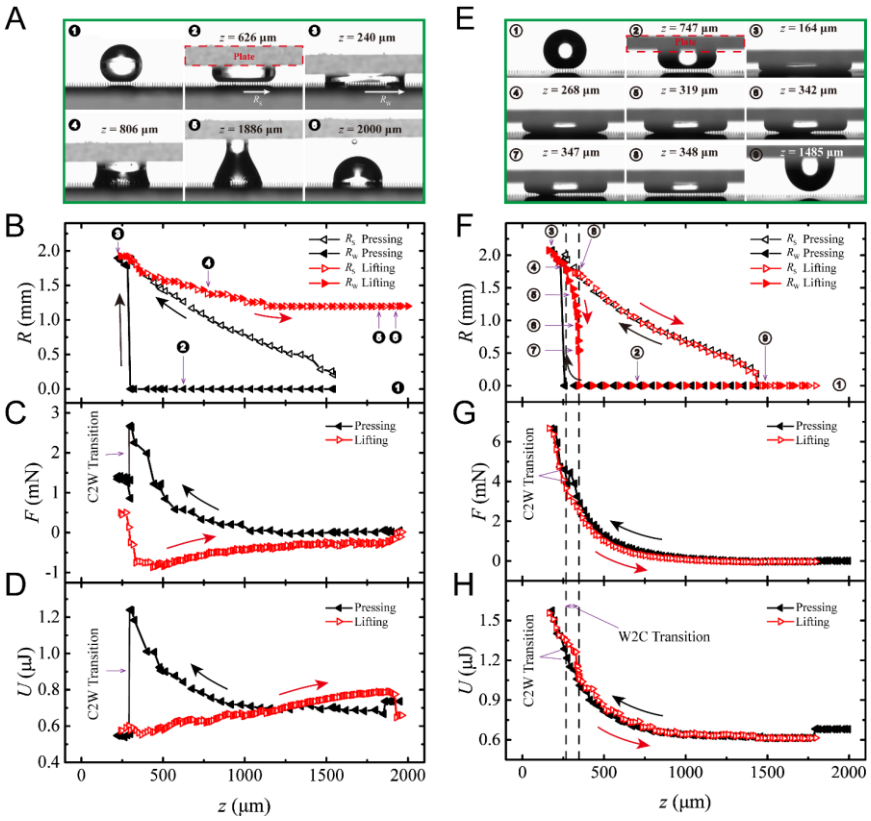

Fig. S10. States, contact radii, force and energy variations for a drop squeezed against a textured surface. Data are full and black in the pressing stage, and empty and red in the releasing stage. (*A*) Same experiment as Fig. S8*A* except for the top plate, which is characheterized by $\theta_a = 114° \pm 2°$ and $\theta_r = 80° \pm 2°$. Corresponding movie is Movie S7. (*B-D*) Corresponding radii, force and energy. (*E*) Same experiment as Fig. S8*C* with the same top plate as the above. Corresponding movie is Movie S8. (*F-H*) Corresponding radii, force and energy.

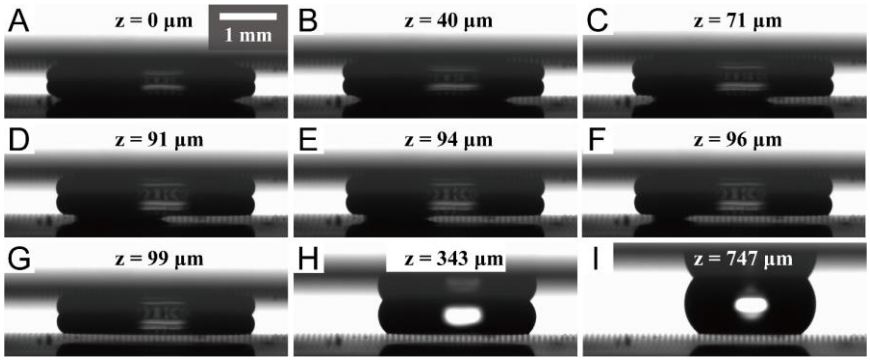

Fig. S11. W2C transition for a glycerol drop with diameter 1.96 mm on a pillar-structured silicon substrate coated with FOTS-coated Glaco. The plate is lifted at a constant speed of 20 µm/s. The transition starts from the drop-substrate contact line (*A*), and liquid within the structures gradually retracts, dewetting the pillars one by one (*B*-*F*), until the final dewetting (*G*). Further lifting the plate does not affect the Cassie state (*H*-*I*).

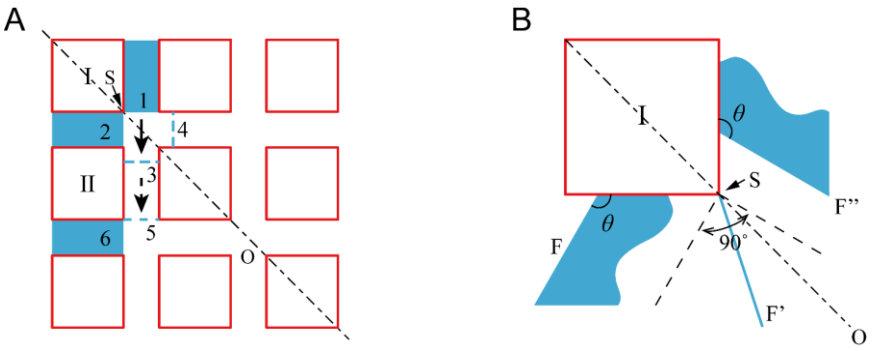

Fig. S12. (*A*) Schematic of how the Cassie state progresses during W2C transition. (*B*) Contact line pinning at sharp edge S.

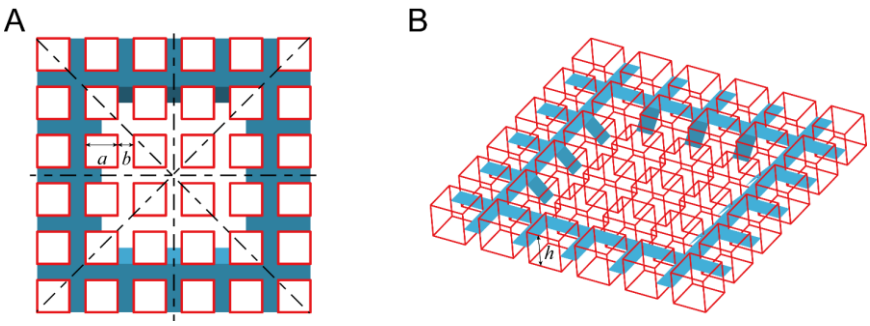

Fig. S13. The starting point of the simulation. The liquid is in the Wenzel state at the center of the domain, and the Cassie state is characterized by the pressence of blue stripes. (*A*) Top view. The dash-dotted lines are the symmetry planes of the configuratioin. (*B*) Perspective view. Red frames indicate pillars, and blue stripes show the liquid-air interfaces. Pillar walls and liquid-solid interfaces are not shown for the sake of clarity.

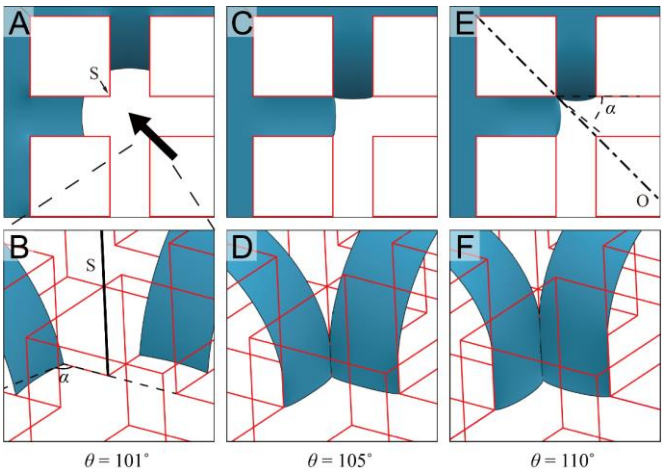

Fig. S14. Equilibrium shape of the menisci at different contact angles, as provided from Surface Evolver. Pillar parameter are $a = 2b$ and $h = a$. (*A-B*). Top and side views of the menisci for $\theta = 101°$. The meniscus is concave, and does not reach the sharp edge S of the pillar. (*C-D*). Top and side views of the menisci for $\theta = 105°$. As the menisci reach the edge S, they get pinned. However, the condition of an obtuse contact angle with the bottom makes them protrude outwards, which favors merging. (*E-F*). Top and side views of the menisci for $\theta = 110°$. The menisci become more convex since the contact angle is higher so that they merge even more easily.

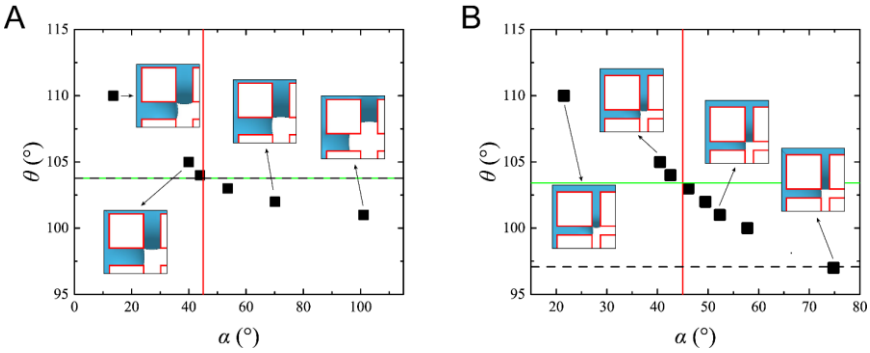

Fig. S15. Relationship between α and θ. α is measured from simulated interfaces at equilibrium. Inserts are top views of the shape of the menisci, and the horizontal dashed line is the critical θ given by **Eq. 1**. The solid green line shows the value of $\theta(45°)$, that is, the value at which contact line may depin from edges. (*A*) $a = 2b$ and $h = a$, corresponding to $f = 0.44$. (*B*) $a = 4b$ and $h = a$, corresponding to $f = 0.64$.

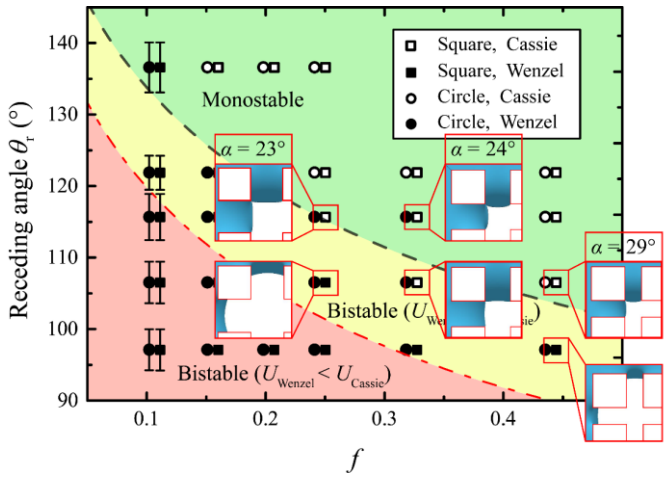

Fig. S16. A few examples of the value of α found from the simulation for the experiments corresponding to the phase diagram in Fig. 4. A is always smaller than 45°, so that **Eq. 1** only is enough to predict the position of W2C transtion.

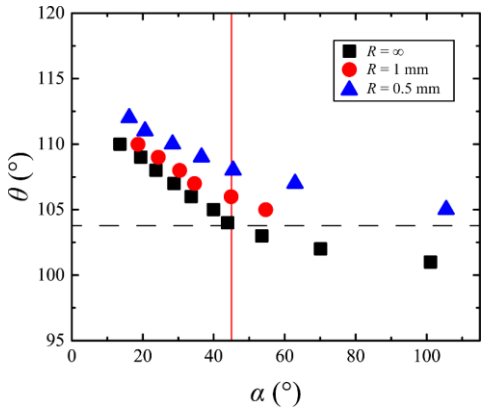

Fig. S17. Pressure influence on α as a function of θ when $a = 2b$ and $h = a$ ($f = 0.44$). Black squares correspond to drops with infinite radii (Laplace pressure equals zero). Red circles and blue triangles correspond to drops with radii of 1 mm and 0.5 mm, respectively.